ACS APPLIED MATERIALS & INTERFACES

www.acsami.org
Research Article

Influence of Atmospheric Conditions on the Structural Evolution upon Heating of the ZnAl-Layered Double Hydroxide: A Comprehensive *In Situ* Transmission Electron Microscopy Study

Matthias Quintelier, Alexander Zintler, Ryosuke Nakazato, Nataly Carolina Rosero-Navarro, Kiyoharu Tadanaga, and Joke Hadermann*

Cite This: *ACS Appl. Mater. Interfaces* 2025, 17, 38587−38596

Read Online

ACCESS | Metrics & More | Article Recommendations | Supporting Information

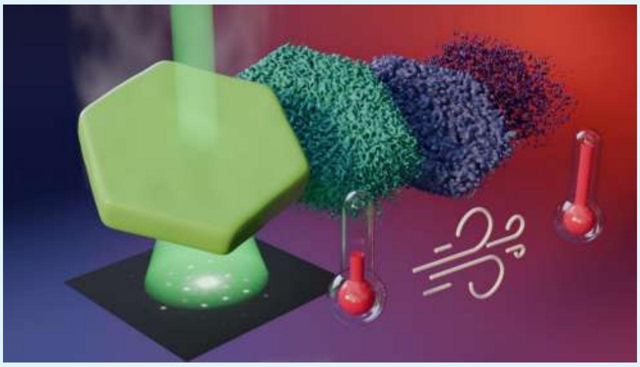

ABSTRACT: Layered double hydroxides (LDHs) are versatile materials with diverse applications, including catalysis, water separation, adsorption, biomedicine, and fire retardancy. This study investigates the thermal evolution of ZnAl LDH ($[Zn^{2+}{}_2Al^{3+}(OH)_6]^+$ $[CO_3{}^{2-}{}_{0.5}]^-$) using *in situ* scanning nanobeam electron diffraction, high-resolution transmission electron microscopy, and energy-dispersive X-ray analysis. The structural and morphological changes are examined during heating in both ambient air and vacuum. The pristine ZnAl LDH exhibited edge dislocations and irregular interlayer distances, leading to significant diffuse scattering in the electron diffraction patterns. Both upon heating in ambient air conditions and in vacuum, the characteristic hexagonal LDH morphology transformed into a porous nanostructure. The exact crystal structure transitions differed as a function of the environment. Heating under vacuum conditions first led to a $ZnAl_2O_4$ phase with a spinel-type structure, and subsequently to ZnO particles embedded within an Al_2O_3 matrix. When heated in a closed cell filled with ambient air, the LDH initially transitioned to an Al-doped ZnO-type structure, followed by conversion to a $ZnAl_2O_4$ phase. This study is the first gas *in situ* TEM LDH study and shows the recrystallization behavior of the LDH into the different phases upon heating and uncovers the nanoscale distribution of these phases within the particles, forming $ZnAl_2O_4$, ZnO, and Al_2O_3 composites.

KEYWORDS: *in situ, TEM, layered double hydroxide, heating, phase transformation*

INTRODUCTION

Layered double hydroxides (LDHs) are a class of anionic clays that have gained significant attention in materials science due to their unique structural characteristics and wide range of applications.

LDHs are represented by the general formula:

$$[M^{2+}{}_{1-x}M^{3+}{}_x(OH)_2]^{x+}[A^{n-}{}_{x/n}]^{x-}\cdot mH_2O \tag{1}$$

where M^{2+} and M^{3+} are divalent and trivalent metal cations, respectively, A^{n-} are the interlayer anions and x is the fraction of the M^{3+} cation, defined as $x = M^{3+}/(M^{2+} + M^{3+})$. The structure of LDHs consists of layers of metal hydroxides, similar to the brucite mineral $Mg(OH)_2$, with interlayer spaces filled with anions and water molecules, as shown in Figure 1. The distance between two LDH layers is known as the basal spacing (Figure 1). This layered structure gives LDHs high anion exchange capacities and the ability to intercalate a variety of molecules, making them highly adaptable for numerous applications. The specific cations used in LDHs significantly influence their suitability for different applications, such as water separation,[1−3] chemical and electromagnetic absorption[4−6] and ion exchange.[7,8] LDHs are also utilized in biomedical applications,[9,10] catalysis[11,12] and environmental remediation.[13−15]

The calcination, with typical temperatures between 400 and 1000 °C, of LDH materials has gained attention from both applied and fundamental research perspectives.[16−21] In general, calcined LDHs are used in applications such as oxygen evolution reactions[22] and as catalytic supports.[23] The formation of metal oxides and spinel-type composites through calcination enhances catalytic performance in various fields, including nanocatalyst design,[24,25] hydrogenation,[26] photocatalysis,[27] and flame retardancy.[28−32] Therefore, understand-

Received: February 17, 2025
Revised: June 3, 2025
Accepted: June 8, 2025
Published: June 18, 2025

https://doi.org/10.1021/acsami.5c03313

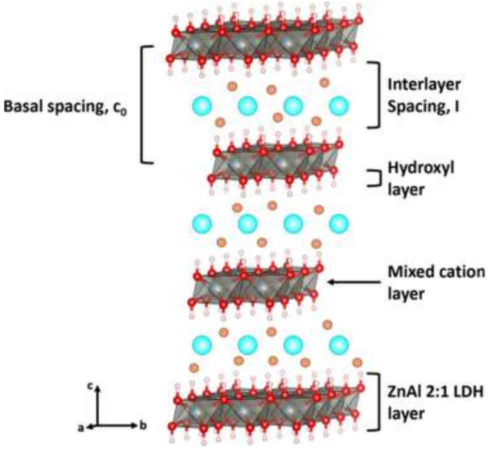

Figure 1. Structure of ZnAl (2:1) LDH. The brown spheres represent interlayer H_2O and the blue speres represent interlayer CO_3^{2-}. The red spheres represent O, the pink ones H, and the gray/blue spheres Zn and Al on a shared position.

ing the structural evolution and morphological modification at elevated temperatures is essential, as it directly influences their performance and stability in the various applications.

An *in situ* heating TEM study on MgAl and NiFe LDHs demonstrated their thermal transformation into α-Al_2O_3 + $MgAl_2O_4$ and NiO + $NiFe_2O_4$, respectively.[33] However, this study was conducted using transmission electron microscopy under high vacuum conditions, whereas realistic applications typically occur in ambient atmospheres, decreasing the representativity of the results. Furthermore, the study focused on the end products, neglecting the intermediate phases that arise during thermal evolution.

Recently, ZnAl LDHs have shown considerable promise in (electro-) catalysis,[34−37] particularly for the selective reduction of CO_2 to CO which is a crucial step in producing hydrocarbons that serve as intermediates for various downstream processes.[38,39] Furthermore, ZnAl LDHs have shown promising use in flame-retardant systems,[40,41] while their calcination products have been employed in dye adsorption,[42] photocatalytic applications,[43] and water purification processes.[44] For ZnAl LDH, *ex situ* and *in situ* XRD studies revealed that the structure gradually starts to collapse at 120 °C, forming a layered double oxide (LDO), which subsequently transforms into a mixture of ZnO and Al_2O_3 or ZnO and $ZnAl_2O_4$ at higher temperatures (900 °C).[45,46] However, the XRD studies do not yield any information on the distribution of the phases, for example their occurrence as single phase versus multiphase particles, or the microstructure (intergrowths, core−shell, distributed nanodomains in a matrix,···). *In situ* TEM offers the unique capability to resolve such nanoscale distributions and phase intergrowths. Moreover, the use of a controlled gas environment in the TEM, instead of the standard vacuum, represents a methodological advancement not previously reported for LDH materials.

This work is the first to reveal the nanoscale crystal structure, morphology and composition of LDHs upon heating in a relevant ambient atmosphere, which is accomplished through the use of *in situ* TEM. The results show not only the structural transformations and degradation pathway of ZnAl LDH, but also that calcination can be used to synthesize the obtained nanocomposites, which are complicated to obtain using the current known routes. These nanoscale insights into phase evolution, morphology, and distribution are not accessible via bulk techniques such as PXRD due to limitations imposed by crystallite size, phase overlap, and signal averaging.

■ RESULTS

Pristine LDH. The pristine ZnAl LDH particles had the characteristic tabular hexagonal morphology of LDHs, resulting clear hexagonal shaped particles when projected parallel to the *c*-axis and giving the faulty impression of needle shapes when projected perpendicular to the *c*-axis (low magnification TEM in Figure S2).The pristine starting material is identical to the one used in the paper by Nakazato et al. (*CO_2Electrochemical Reduction with Zn−Al Layered Double Hydroxide-Loaded Gas-Diffusion Electrode. Electrochemistry 2023.* 10.5796/electrochemistry.23-00080), which provides the XRD pattern, also shown in Figure S9, showing no indication of any secondary phases for the pristine sample. STEM-EDX analysis confirmed the targeted cation ratio, with Zn:Al = 2.0(2) (Figure S3, Table S1). Low dose HRTEM (Figure S4) showed that the spacing between consecutive mixed cation layers varies over nanoscale regions with an average basal spacing c_0 = 7.4(6) Å. This variation causes diffuse scattering in the SAED patterns (Figure 2a).

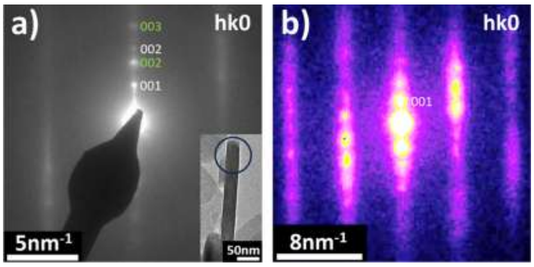

Figure 2. (a) SAED pattern taken using the smallest possible SAED aperture. Irregular basal spacings cause the presence of diffuse scattering. Two basal spacings dominate in this SAED image, indexed in white and green. The inset shows the studied particle, along with the area used for the SAED pattern. (b) Diffraction pattern obtained using SNBD. The small beam size (∼5 nm) produces local diffraction patterns, minimizing the diffuse scattering.

Although conventional PXRD indicated a perfect crystal with no detectable defects or layer variations,[38] HRTEM imaging showed irregular basal spacing, in agreement with the electron diffraction patterns, and edge dislocations. (Figure S5).

Figure 3a shows a representative area from a scanning nanobeam electron diffraction (SNBD) scan, showing particles that contain the c*-axis on the diffraction patterns. The SNBD technique employs a small, 5 nm semiparallel probe that scans across the particles, capturing a diffraction pattern at each scan position. This method provides local structural information at each point and reduces the amount of diffuse scattering in the diffraction patterns, as shown in Figure 2b. Figure 3b displays the variation in basal spacing across scan points. Performing the basal spacing analysis like this not only provides an average basal spacing but also reveals nanoscale variations, which causes the diffuse scattering observed in Figure 2a. Specifically, at the edges the basal spacing is consistently lower than in the core of the particles. Possibly, the vacuum environment causes the removal of a certain amount of molecules along the edges. The average basal spacing obtained from SNBD is 7.2(2) Å,

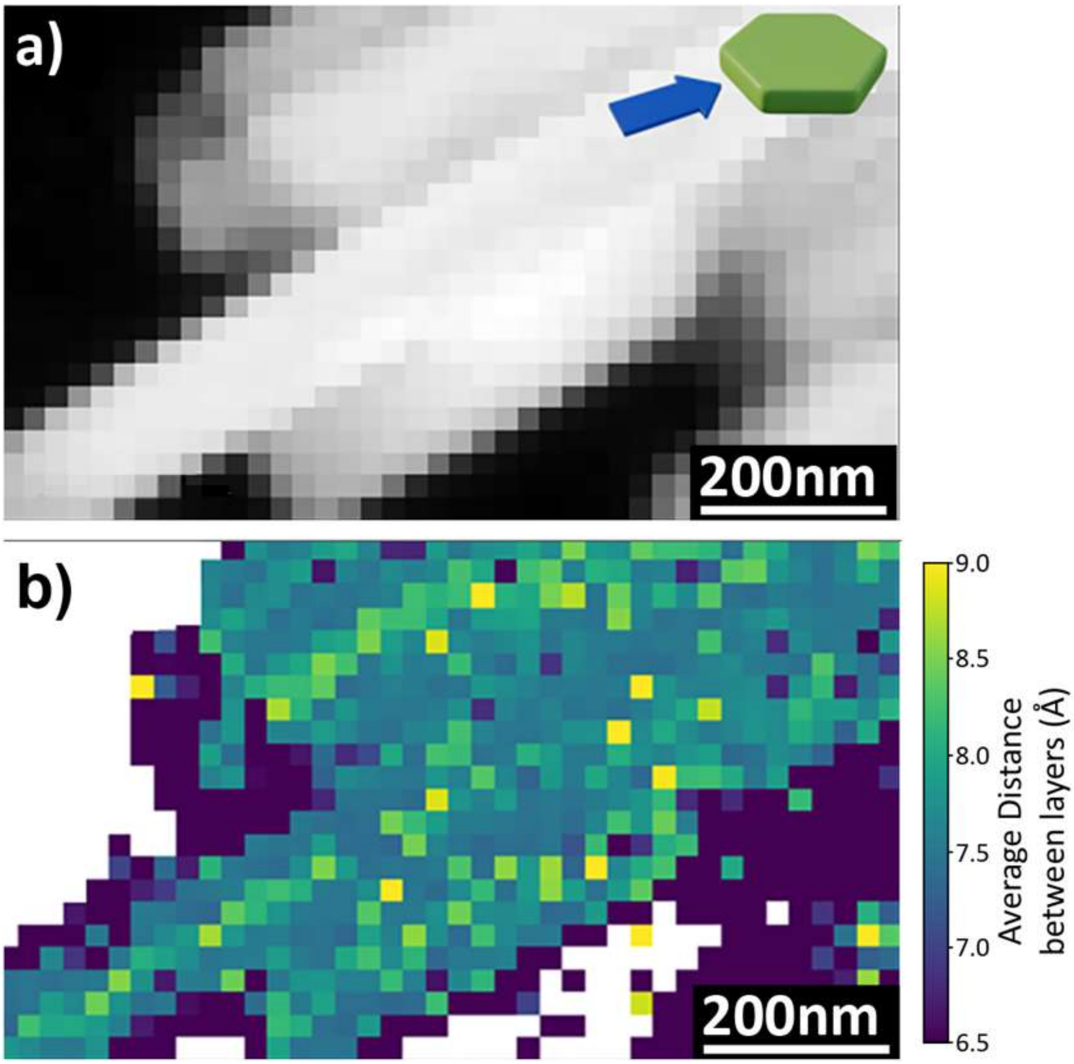

Figure 3. (a) SNBD scan of particles that are lying in an orientation where the diffraction pattern contains the *c**-axis of the material, making it possible to study the basal spacing. The inset shows a schematical representation of the viewing direction. (b) Map of the variations in basal spacings per scan point of (a).

which is within range of the average basal spacing obtained from HRTEM.

Heating in Vacuum. When heating the ZnAl LDH particles in vacuum, the HAADF-STEM images (Figure 4a) show a slightly rougher appearance at 200 °C than at 20 °C. The average basal spacing at 200 °C has decreased to 5.0(8)Å (Figure S6) when measured from HRTEM, while SNBD shows two separate basal spacings, corresponding with 7.27 Å and 5.71(5) Å. (Figure S7). According to literature, such reduction of the basal spacing is due to the dehydration of the LDH; the decomposition of the CO_3^{2-} interlayer anions and the decomposition of the hydroxide layers adjacent to the cation layers.[47] The difference in exact values between the basal spacings at the same temperature from HRTEM versus SNBD could be due to local differences. The variation in basal spacings could not be mapped (as done higher for the pristine material) due to the material's low crystallinity. SNBD taken along the [001] zone axis shows the same reflections at 200 °C as at 20 °C, indicating that the LDH structure is still retained up to 200 °C. The higher order reflections have become weaker, corresponding to a decrease in crystallinity. Pores start to form at 400 °C, clearly visible on the HAADF-STEM images (Figure 4a) and increase in size upon further heating. A close-up of the pores is shown in Figure 4b. After the full heating curve, the sample was cooled down to 650 °C (as HAADF-STEM imaging at 950 °C was impossible due to the increased beam damage) and high resolution HAADF-STEM images (Figure 4c) were taken while monitoring the Kikuchi lines at a single point to ensure structural stability. These HAADF-STEM images confirm that the dark regions in Figure 4a are effectively pores.

Phase maps were made by matching the local electron diffraction patterns obtained by SNBD to a database of calculated electron diffraction templates via the ASTAR software suite.[48,49] Representative electron diffraction patterns of a single 5 nm scan point within the map are shown below the phase maps to clarify that the different phases can be clearly distinguished. Phase mapping using the SNBD data (Figure 5) shows that the LDH structure is still homogeneously present over the whole particle at 200 °C. At 400 °C the particle has the $ZnAl_2O_4$ structure. By 650 °C, Al_2O_3 has appeared within the $ZnAl_2O_4$ matrix. At 850 °C, the phase map indicates mostly ZnO within an Al_2O_3 matrix. Minute traces of the spinel phase $ZnAl_2O_4$ are still present and some locations

https://doi.org/10.1021/acsami.5c03313
ACS Appl. Mater. Interfaces 2025, 17, 38587−38596

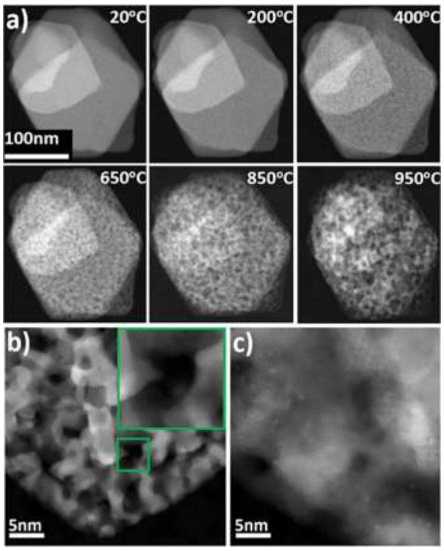

Figure 4. (a) HAADF-STEM images showing the morphological changes of an LDH particle. Starting from 400 °C, the morphology changes to a porous structure. (b, c) High-magnification HAADF-STEM images of the structure formed after heating ZnAl (2:1) to 950 °C and cooldown to 650 °C in vacuum.

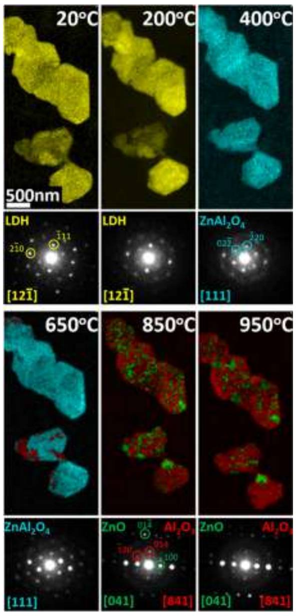

Figure 5. Phase maps of the same particle at the different heating stages. We observe a phase transformation of the LDH structure (yellow) to $ZnAl_2O_4$ (light blue) and then further to ZnO (green) in an Al_2O_3 (red) matrix. The Al_2O_3 phase starts to form at 650 °C. The presence of Zn particles (dark blue) at 850 and 950 °C is also observed. Underneath each phase map, a diffraction pattern of one manually selected 5 nm area within the SNBD scan during the heating curve, along with manual indexations of the patterns and zone identifications.

with pure Zn are observed. After heating to 950 °C, no spinel phase was observed anymore, while ZnO has diffused more inward and aggregated into larger domains. All of these phases correspond to the stable phases shown in the Zn−Al−O phase diagram (Figure S8), however, it was unknown how they were distributed throughout the particles.

The phase maps do not show the pores because they are initially smaller than the 5 nm beam used for the scans and for the higher temperatures the pores do not pass all the way through the material. Thus, for each scan point the diffraction pattern will be that of the remaining material within this 5 nm probe area.

The changes in the particles during heating were also followed using HRTEM. Note that for each technique fresh particles were studied, to avoid beam damage. While at low temperatures only the basal spacings change as mentioned above, at 850 °C new crystalline domains appeared on the HRTEM images (Figure 6). Analysis of the interplanar distances of these domains indicated *d*-spacings corresponding to the (110) planes of the Al_2O_3 phase. This is in agreement with the increasing amount of Al_2O_3 on the phase maps. On the HAADF-STEM images (Figure 4a), the domain formation is not clear, as the pores dominate the appearance of the particle.

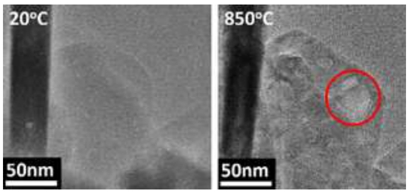

Figure 6. HRTEM images showing formation of crystalline domains at 850 °C (indicated by a red circle), with interplanar distances corresponding to the (110) planes of the Al_2O_3 structure, upon heating in vacuum. The contrast for these images was enhanced by taking the Fourier transform, applying a mask to the two visible spots in the frequency domain, performing an inverse FFT, and overlaying the resulting image with the original one.

No formation of LDO was observed during heating, although it was reported in literature to form at 120 °C.[46] This discrepancy can likely be attributed to the expected poor crystallinity of LDO.[50,51] In this regard it is important to note that when diffraction patterns consist of two overlapping patterns from different phases, the phase mapping software assigns the phase of the most intense pattern, which makes nanometer scaled, poorly crystalline phases difficult to detect.

After heating, the particles were allowed to cooled down, after which STEM-EDX measurements were taken (Figure 7a).

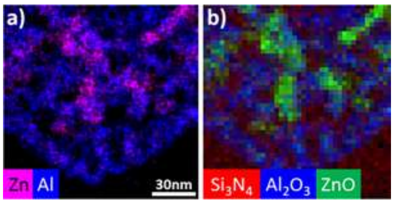

Figure 7. (a) STEM-EDX elemental map showing the Zn and Al content. The map is given in counts. (b) Component map from NMF analysis.

STEM-EDX showed areas rich in Zn and O within a matrix composed of Al and O (for clarity, O has been excluded from the maps in Figure 7a. However, the Si_3N_4 background makes the composition determination of these regions impossible using standard EDX processing techniques. Therefore, PCA combined with NMF analyses, as outlined in,[52] is used. This confirms that these regions are indeed Al_2O_3 and ZnO (Figure

7b and Table S2). This confirms that ZnO particles form within an Al_2O_3 matrix as found using SNBD (Figure 6).

Heating in Atmospheric Conditions. To explore the impact of the atmosphere on the structural evolution of the particle, we investigated the crystal structure with the same heating curve, but in ambient air. For these ambient conditions, we first also performed powder X-ray diffraction (Figure S9) during heating, which shows the disappearance of the characteristic LDH peaks around 150 °C, and the appearance of ZnO peaks around 200−250 °C. Starting at 150 °C, all peaks are low and broad, and further information about any phases could not be derived. This agrees with the following TEM study, which shows that, upon heating, the crystallinity decreases, and the particles become multiphased with nanoscale domains. Therefore, further analysis was performed using TEM as this technique allows to gather information at nanoscale spatial resolution.

Heating in air produced a similar porous morphology to that observed when heating in vacuum (Figure 8), with the porous structure emerging at 400 °C but being less pronounced than in vacuum. However, as shown further on in this section, the phase composition differs.

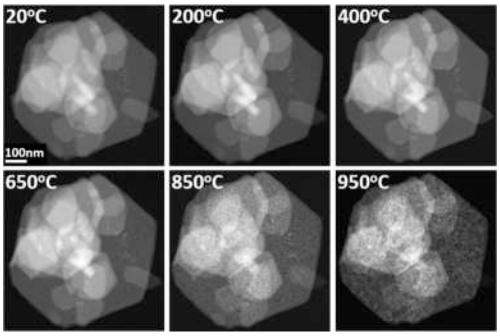

Figure 8. HAADF-STEM images showing the morphological changes of an LDH particle upon heating in air. Starting from 400 °C, the morphology changes to a porous structure.

Using SNBD, again a manually selected, representative 5 nm area was followed throughout the heating curve, which showed that also in air the LDH structure is mostly retained up to 200 °C (Figure 9). Phase maps based on an SNBD scan of the entire particle reveal the presence of ZnO domains at 200 °C (Figure 9). The in-house code could not be applied to these data sets because particles showing the c*-axis were overlapped by others in different orientations. This overlap produced additional spots in the diffraction patterns, which were visible in the line profiles and affected the measured distances by the code. Furthermore, as observed in data sets taken at 200 °C, the particles' low crystallinity resulted in poorly defined peaks in the line profiles, rendering them unsuitable for the code.

At 400 °C, the main phase is identified as ZnO by the SNBD technique. At 650 °C, $ZnAl_2O_4$ domains arise as a secondary phase. However, if at 400 °C the particles would be pure-phase ZnO, this would imply a disappearance and reappearance of the element Al. Therefore, to locate the Al, we conducted STEM-EDX analysis at 400 and 650 °C (Figure 10), which shows that Al is uniformly distributed throughout the particle. Since the diffraction patterns correspond to the ZnO crystal structure, the Al atoms should be present as in a (Zn,Al)O solid solution. At 850 °C, $ZnAl_2O_4$ dominates the particle, with only few domains of ZnO remaining. At 950 °C, only $ZnAl_2O_4$ is observed. All of these found phases correspond to the stable phases shown in the Zn−Al−O phase diagram, see Figure S8, however, also here, it was not known how these phases were distributed over the particles.

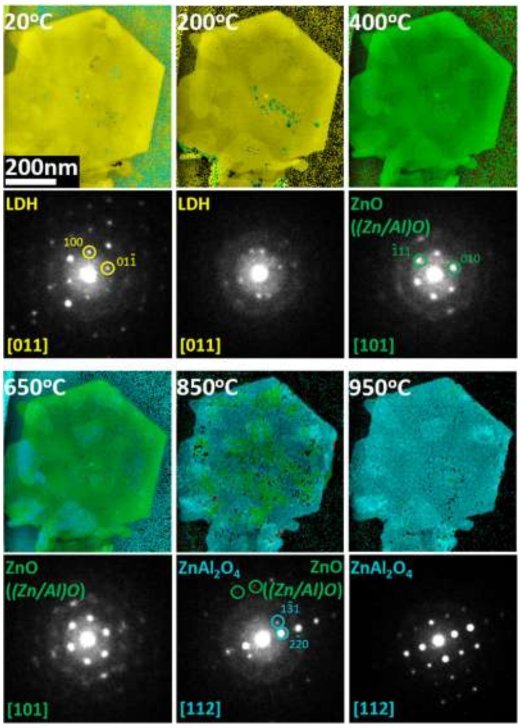

Figure 9. Phase maps of the same particle at different temperatures. Underneath each phase map, a diffraction pattern is shows of one representative scan point (5 nm area) within the map, manually indexed. Note that the ZnO phase is found to be (Zn,Al)O using STEM-EDX afterward.

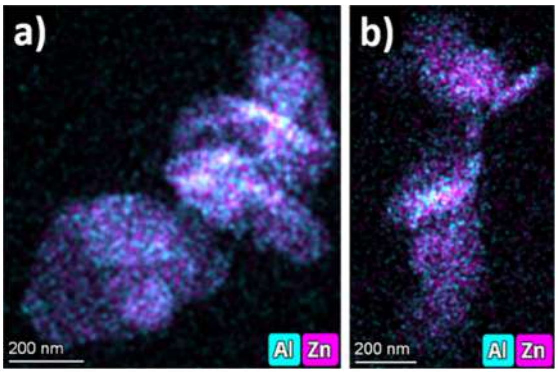

Figure 10. STEM-EDX maps in net counts showing the homogeneous Zn and Al content of particles at (a) 400 and (b) 650 °C.

After the full heating curve in air, STEM-EDX (Figure 11a) shows a homogeneous distribution of Zn, Al and O over the particles, in agreement with the phase maps showing only a single phase. Standard NMF analysis was unable to separate the Si_3N_4 signal of the cell windows from the particle signal due to the low number of counts and the high fluorescence of the Zn signal compared to the one from Si. Therefore, we employed principal component analysis (PCA) combined with blind source separation (BSS) using independent component analysis (ICA) to identify the components in the data set

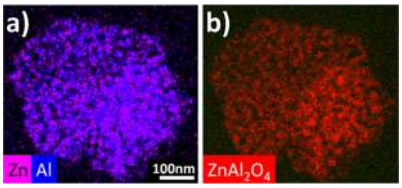

Figure 11. (a) STEM-EDX elemental map showing the Zn and Al content. The map is given in counts. (b) Component map produced by the BSS analysis. The Si_3N_4 background is not shown as a separate component.

(Figure 11b). This analysis revealed only a single component, agreeing with $ZnAl_2O_4$, within the particles (Table S3).

DISCUSSION

Table 1 shows a summarizing table of the observed key (structural) features per utilized experimental technique. The combination of (Zn,Al)O/$ZnAl_2O_4$ offers enhanced effectiveness in applications like dye degradation.[53,54] However, synthesizing nanometer scale composites of this combination is challenging, with for example sol−gel processes struggling to produce both phases in a single particle.[55,56] The results in the current paper demonstrate that heating ZnAl LDH in air produces the (Zn,Al)O/$ZnAl_2O_4$ phase combination at lower temperatures than previously reported.[57,58] Moreover, these phases are observed to coexist within nanometer-sized particles with a porous structure, revealing their distribution at the nanoscale. These findings show the important role of nanoscale characterization in understanding material behavior. By combining SNBD with *in situ* gas-environment TEM, we achieve spatial and structural resolution beyond the capabilities of conventional techniques like PXRD, enabling the study of thermally sensitive and compositionally complex materials under more realistic conditions.

Furthermore, ZnO/Al_2O_3 composites, require advanced synthesis techniques like atomic layer deposition,[59,60] while $ZnAl_2O_4$ synthesis potentially demands high-temperature heating.[61] Both are promising for catalytic applications.[62,63] Here, low temperature heating of the ZnAl LDH in vacuum resulted in $ZnAl_2O_4$, while higher temperature calcination resulted in ZnO/Al_2O_3 composites.

Heating ZnAl LDH in vacuum and air thus provides alternative routes for synthesizing $ZnAl_2O_4$, and ZnO/Al_2O_3 and (Zn,Al)O/$ZnAl_2O_4$ composites. Traditional synthesis methods, such as atomic layer deposition for ZnO/Al_2O_3 or high-temperature heating for $ZnAl_2O_4$, are more complex and resource-intensive than the easy synthesis of the LDH particles, combined with their calcination.

The difference in outcomes, caused by varying atmospheres, underscores the need to examine the structural evolution of these materials under conditions reflective of their real-world applications. This emphasis on simulating practical usage environments is crucial for gaining accurate insights into material behavior and optimizing their performance for potential applications. Understanding the precise structural evolution of ZnAl LDH during heating is critical for optimizing catalytic and thermal performance, as each phase—whether $ZnAl_2O_4$, Al-doped ZnO, or ZnO in an Al_2O_3 matrix—has distinct electronic, catalytic, and thermal properties that directly influence material stability, reactivity, and durability. If the wrong phase transition pathway is assumed, materials may be designed with unintended phases that lack the necessary characteristics, leading to reduced catalytic efficiency, faster degradation, or inadequate performance in target applications.

While PXRD showed the formation of ZnO after heating the material in air above 250 °C, with this phase remaining dominant up to 500 °C, the nanoscale dimensions of the particles limit the suitability of XRD for detailed structural characterization.

Although all these phases are documented in the literature and the Zn−Al−O phase diagram, the observed distribution of elements and the formation of a unique morphology were unknown. These could only be accurately characterized by employing *in situ* TEM for accurately mapping these transformations under different atmospheres.

CONCLUSIONS

The structural and morphological evolution of ZnAl LDH upon calcination in air and in vacuum was investigated using *in situ* transmission electron microscopy. This comprehensive study sheds light on the intricate phase transformations, crystallization pathways and structural dynamics underlying the structural and morphological evolution of LDHs on a nanometer scale. Heating the ZnAl LDH particles in air results in a phase transition via (Zn,Al)O and a (Zn,Al)O/$ZnAl_2O_4$ composite into $ZnAl_2O_4$, whereas heating the LDH particles in vacuum results via $ZnAl_2O_4$ and a $ZnAl_2O_4$/Al_2O_3 composite in ZnO particles within an Al_2O_3 matrix. The particles are porous at 400 °C and higher temperatures.

Table 1. Table Summarizing Key Features Observed per Experimental Technique

	observed (structural) features		
technique	pristine LDH	heating in vacuum	heating in air
(SA)ED	significant diffuse scattering indicating irregular basal spacings		
HRTEM	irregular basal spacings	formation of unidentified crystalline nanoparticles at 850 °C	
SNBD	irregular basal spacing	phase transformation: LDH (20 and 200 °C) $ZnAl_2O_4$ (400 °C) $ZnAl_2O_4$ + Al_2O_3 (650 °C) Al_2O_3 + ZnO (850 and 950 °C)	phase transformation: LDH (20 °C) LDH (+ (Zn, Al)O) (200 °C) (Zn,Al)O (400 °C) (Zn,Al)O + $ZnAl_2O_4$ (650 and 850 °C) $ZnAl_2O_4$ (950 °C)
HAADF-STEM	hexagonal particle morphology	formation of porous structure at 400 °C, size of the pores increasing with temperature	
STEM-EDX	ZnAl 2:1 cation ratio	end phase Al_2O_3 and ZnO composite.	end phase $ZnAl_2O_4$; homogenous distribution of Al throughout the particles at 400 and 650 °C

https://doi.org/10.1021/acsami.5c03313
ACS Appl. Mater. Interfaces 2025, 17, 38587−38596

EXPERIMENTAL SECTION

Synthesis and Initial Characterization of ZnAl LDH. Zn Al LDH with CO_3^{2-} anions was prepared using a facile and traditional coprecipitation process as shown in Figure S1. An aqueous solution containing $Zn(NO_3)_2 \cdot 6H_2O$ and $Al(NO_3)_3 \cdot 9H_2O$ with Zn^{2+}/Al^{3+} = 2.0 was added dropwise into a 0.30 M aqueous Na_2CO_3 solution with stirring at 80 °C. The drop rate was adjusted to 2 mL min^{-1} by using a syringe pump. The pH of the reaction mixture was adjusted to 10 by adding 2.0 M aqueous NaOH solution with a pH meter. The obtained solution was aged at room temperature for 24 h. The resulting white precipitates were filtrated, washed with distilled water, and dried at 80 °C for 24 h. This synthesis and XRD characterization of the material is also described in.[38]

TEM Characterization. High resolution transmission electron microscopy (HRTEM), selected area electron diffraction (SAED) and high angle annular dark field scanning transmission electron microscopy (HAADF-STEM) experiments were conducted on probe- and/or image-corrected Titan transmission electron microscopes (Thermo Fisher, Eindhoven, Netherlands), operated at 300 kV. The semiconvergence angle for the HAADF-STEM experiment was 21 mrad. A Gatan K2 Summit direct electron detector was used for the HRTEM experiments. Overview TEM images were taken with a US1000 CCD camera.

For SNBD (scanning nanobeam electron diffraction), a Quantum-Detectors MerlinEM 1R direct electron detector (DED) was used. STEM-EDX maps were acquired using a SuperX-EDX detector. Special care was taken to avoid electron beam damage to the particles: the beam was blanked when not taking an image and a low total dose (<50 $e^-/Å^2$) was used for the HRTEM experiments. The HRTEM images presented in this study are the result of a series of low dose images that were drift corrected and then summed. The SNBD scan was performed with a dwell time of 822 μs using the 2 × 12 bit counter mode of the Merlin DED.

The sample was heated in vacuum using a Wildfire holder with Nano-Chip MEMS (micro electromechanical systems), and was heated in air using a Climate holder with Nano-Reactor MEMS, all manufactured by DENSsolutions (Delft, Netherlands). Nano-Chips for heating the sample are open chips, exposing the material to the ultrahigh vacuum of the microscope, which is typically around 1.18.10^{-5} Pa. In contrast, Nano-Reactors consist of top and bottom chips separated by an O-ring, forming a sealed cell at the holder's tip. To achieve standard ambient pressure in air, the valves of the Climate holder were open to the room's atmosphere. A 5 nm amorphous carbon coating was applied to the back of both types of chips using a Leica (Wetzlar, Germany) carbon coater to prevent charging of the MEMS devices, which could otherwise induce structural changes or cause particle displacement.

HRTEM simulations were conducted using Recipro software version 4.890.[64] Phase mapping was performed using the programs in the ASTAR software suite (DiffGen version 2.0.10.960, INDEX version 2.0.10.1552 and MapViewer version 2.0.10.474). The structures used for this mapping were Al_2O_3 (ICSD 9770[65]), NiCo LDH (ICSD 11988[66]), where Ni was substituted for Zn and Co for Al), and $ZnAl_2O_4$ (ICSD 39473[67]). Structures for Al[68] and Zn[69] were obtained from the CrystalMaker database, while the ZnO structure was sourced from the Crystallography Open Database (COD 1011258[70]). STEM-EDX (energy dispersive X-ray analysis) data processing was done using ESPRIT (Bruker, version 1.9.4.3337) and VELOX (Thermo Fisher, version 3.11.0.1114–60f131bdob) software. Non-negative matrix factorization (NMF) and blind source separation (BSS) analyses of the STEM-EDX data were performed using the Python packages Hyperspy[71] and Pyxem,[72] following the methodologies described in.[52]

An in-house written Python code utilizing HyperSpy and Pyxem was used to investigate the local basal spacings at each probe position in a SNBD scan. For regions-of-interest (ROI) containing the material's c*-axis, a line profile along the 00l row of reflections in diffraction space was defined for each probe position. This line profile was smoothed by upscaling with a third-order polynomial interpolation between points, and local maxima were identified using a minimum intensity threshold to reduce noise interference. Local maxima corresponding with a similar spacing were considered to belong to a single c* value. The distances between these local maxima were averaged for each line profile to determine the average basal spacing at each scan point.

The heating curve that was followed for all experiments, both for heating in vacuum and for heating at ambient conditions is shown in Figure 12.

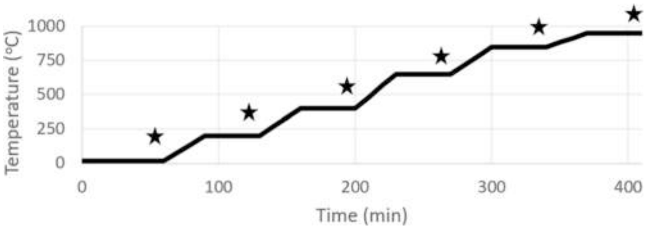

Figure 12. Heating curve followed for all experiments. The stars indicate the temperatures and times where the data was acquired.

ASSOCIATED CONTENT

Supporting Information

The Supporting Information is available free of charge at https://pubs.acs.org/doi/10.1021/acsami.5c03313.

Schematic illustration of the synthesis of ZnAl (2:1) LDH, BFTEM images and STEM-EDX maps of pristine ZnAl (2:1), HRTEM images showing irregular basal spacings, HRTEM simulations, all HRTEM images when heating in vacuum, SNBD patterns at 20 and 200 °C, NMF & BSS results and explanations, ZnAlO phase diagram; PXRD patterns of ZnAl (2:1) heated (PDF)

AUTHOR INFORMATION

Corresponding Author

Joke Hadermann − *EMAT, Department of Physics, University of Antwerp, Antwerp 2020, Belgium;* orcid.org/0000-0002-1756-2566; Email: joke.hadermann@uantwerpen.be

Authors

Matthias Quintelier − *EMAT, Department of Physics, University of Antwerp, Antwerp 2020, Belgium;* orcid.org/0000-0003-0206-0261

Alexander Zintler − *EMAT, Department of Physics, University of Antwerp, Antwerp 2020, Belgium*

Ryosuke Nakazato − *Faculty of Engineering, Hokkaido University, Sapporo, Hokkaido 060-8628, Japan*

Nataly Carolina Rosero-Navarro − *Instituto de Cerámica y Vidrio, ICV-CSIC, Madrid 28049, Spain;* orcid.org/0000-0001-6838-2875

Kiyoharu Tadanaga − *Faculty of Engineering, Hokkaido University, Sapporo, Hokkaido 060-8628, Japan;* orcid.org/0000-0002-3319-4353

Complete contact information is available at: https://pubs.acs.org/10.1021/acsami.5c03313

Author Contributions

Conceptualization was performed by M.Q. and J.H.; methodology was done by M.Q. and J.H.; data processing was performed by M.Q. and A.Z.; formal analysis was done by all authors; material synthesis was performed by R.N., N.C.R.N., and K.T.; investigation was performed by M.Q; resources were gathered by J.H.; writing—original draft preparation—was performed by M.Q. and J.H.; writing—review and editing—was performed by all authors; supervision was done by J.H.; funding acquisition was done by J.H. The manuscript was written through the contributions of all authors. All authors have given approval to the final version of the manuscript.

Funding

EU HORIZON 2020:101022633 FWO Hercules: G0H4316N FWO-Hercules: I003218N BOF TOP 38689.

Notes

The authors declare no competing financial interest.

■ ACKNOWLEDGMENTS

The 4AirCRAFT project has received funding from the European Union's Horizon 2020 research and innovation programme under Grant Agreement No 101022633. This work is supported by Japan Science and Technology Agency (JST) under Grant Agreement No JPMJSC2102. Financial support is acknowledged from the University of Antwerp through BOF TOP 38689. Furthermore, we acknowledge the Hercules fund 'Direct electron detector for soft matter TEM' (FWO-Hercules fund G0H4316N) from Flemish Government for the purchase of the K2 and Merlin DED. We also acknowledge the Hercules fund Infrastructure for imaging nanoscale processes in gas/vapor or liquid environments' (FWO-Hercules fund I003218N) from Flemish Government.

■ ABBREVIATIONS

BSS,blind source separation; DED,direct electron detector; EDX,energy-dispersive X-ray analysis; HAADF,high-angle annular dark field; HRTEM,high-resolution transmission electron microscopy; LDH,layered double hydroxide; NMF,non-negative matrix factorization; PCA,principle component analysis; STEM,scanning transmission electron microscopy

■ REFERENCES

(1) Zhang, Q.; Zhang, G.; Huang, Y.; He, S.; Li, Y.; Jin, L.; Han, J. Surface-Modified LDH Nanosheets with High Dispersibility in Oil for Friction and Wear Reduction. *ACS Appl. Mater. Interfaces* **2024**, *16* (4), 5316−5325.

(2) He, W.; Lin, T.; Song, Z.; Cheng, Y.; Zheng, R.; Chen, W.; Miras, H. N.; Song, Y.-F. Fabrication of Epitaxially Grown Mg$_2$Al-LDH-Modified Nanofiber Membranes for Efficient and Sustainable Separation of Water-in-Oil Emulsion. *ACS Appl. Mater. Interfaces* **2023**, *15* (3), 4755−4763.

(3) Alves, D.; Moral, R. A.; Jayakumari, D.; Dempsey, E.; Breslin, C. B. Factorial Optimization of CoCuFe-LDH/Graphene Ternary Composites as Electrocatalysts for Water Splitting. *ACS Appl. Mater. Interfaces* **2024**, *16* (38), 50846−50858.

(4) Feng, Y.; Li, D.; Wang, Y.; Evans, D. G.; Duan, X. Synthesis and Characterization of a UV Absorbent-Intercalated Zn-Al Layered Double Hydroxide. *Polym. Degrad. Stab.* **2006**, *91* (4), 789−794.

(5) Tang, Z.; Qiu, Z.; Lu, S.; Shi, X. Functionalized Layered Double Hydroxide Applied to Heavy Metal Ions Absorption: A Review. *Nanotechnol. Rev.* **2020**, *9*, 800−819.

(6) Xu, X.; Shi, S.; Tang, Y.; Wang, G.; Zhou, M.; Zhao, G.; Zhou, X.; Lin, S.; Meng, F. Growth of NiAl-Layered Double Hydroxide on Graphene toward Excellent Anticorrosive Microwave Absorption Application. *Advanced Science* **2021**, *8* (5), No. 202002658.

(7) Badreddine, M.; Legrouri, A.; Barroug, A.; De Roy, A.; Besse, J. P. Ion Exchange of Different Phosphate Ions into the Zinc−Aluminium−Chloride Layered Double Hydroxide. *Mater. Lett.* **1999**, *38* (6), 391−395.

(8) Drenkova-Tuhtan, A.; Mandel, K.; Paulus, A.; Meyer, C.; Hutter, F.; Gellermann, C.; Sextl, G.; Franzreb, M.; Steinmetz, H. Phosphate Recovery from Wastewater Using Engineered Superparamagnetic Particles Modified with Layered Double Hydroxide Ion Exchangers. *Water Res.* **2013**, *47* (15), 5670−5677.

(9) Hu, T.; Gu, Z.; Williams, G. R.; Strimaite, M.; Zha, J.; Zhou, Z.; Zhang, X.; Tan, C.; Liang, R. Layered Double Hydroxide-Based Nanomaterials for Biomedical Applications. *Chem. Soc. Rev.* **2022**, *51* (14), 6126−6176.

(10) Kuthati, Y.; Kankala, R. K.; Lee, C. H. Layered Double Hydroxide Nanoparticles for Biomedical Applications: Current Status and Recent Prospects. *Appl. Clay Sci.* **2015**, *112-113*, 100−116.

(11) Wu, H.; Zhang, J.; Lu, Q.; Li, Y.; Jiang, R.; Liu, Y.; Zheng, X.; Zhao, N.; Li, J.; Deng, Y.; Hu, W. High-Entropy Layered Double Hydroxides with Highly Adjustable Components for Enhancing Electrocatalytic Oxygen Evolution. *ACS Appl. Mater. Interfaces* **2023**, *15* (32), 38423−38432.

(12) Liu, Y.; Pei, M.; Liang, H.; Wu, X.; Li, B.; Si, Z.; Kang, F. Rational Design and Preparation of Pt−LDH/CeO$_2$ Catalyst for High-Efficiency Photothermal Catalytic Oxidation of Toluene. *ACS Appl. Mater. Interfaces* **2022**, *14* (32), 36633−36643.

(13) Jijoe, P. S.; Yashas, S. R.; Shivaraju, H. P. Fundamentals, Synthesis, Characterization and Environmental Applications of Layered Double Hydroxides: A Review. *Environmental Chemistry Letters* **2021**, *19*, 2643−2661.

(14) Zhang, R.; Ai, Y.; Lu, Z. Application of Multifunctional Layered Double Hydroxides for Removing Environmental Pollutants: Recent Experimental and Theoretical Progress. *J. Environ. Chem. Eng.* **2020**, *8* (4), No. 103908.

(15) Chaillot, D.; Bennici, S.; Brendlé, J. Layered Double Hydroxides and LDH-Derived Materials in Chosen Environmental Applications: A Review. *Environmental Science and Pollution Research* **2021**, *28* (19), 24375−24405.

(16) Xiao, T.; Tang, Y.; Jia, Z.; Li, D.; Hu, X.; Li, B.; Luo, L. Self-Assembled 3D Flower-like Ni^{2+}−Fe^{3+} Layered Double Hydroxides and Their Calcined Products. *Nanotechnology* **2009**, *20* (47), No. 475603.

(17) Kobayashi, Y.; Ke, X.; Hata, H.; Schiffer, P.; Mallouk, T. E. Soft Chemical Conversion of Layered Double Hydroxides to Superparamagnetic Spinel Platelets. *Chem. Mater.* **2008**, *20* (6), 2374−2381.

(18) Sjåstad, A. O.; Andersen, N. H.; Vajeeston, P.; Karthikeyan, J.; Arstad, B.; Karlsson, A.; Fjellvåg, H. On the Thermal Stability and Structures of Layered Double Hydroxides Mg1− x Alx (OH)2-(NO3)x mH2O(0.18 ≤ x ≤ 0.38). Eur. *J. Inorg. Chem.* **2015**, *2015* (10), 1775−1788.

(19) Xu, W.; Mertens, M.; Kenis, T.; Derveaux, E.; Adriaensens, P.; Meynen, V. Can. High Temperature Calcined Mg−Al Layered Double Hydroxides (LDHs) Fully Rehydrate at Room Temperature in Vapor or Liquid Condition? *Mater. Chem. Phys.* **2023**, *295*, No. 127113.

(20) Magri, V. R.; Duarte, A.; Perotti, G. F.; Constantino, V. R. L. Investigation of Thermal Behavior of Layered Double Hydroxides Intercalated with Carboxymethylcellulose Aiming Bio-Carbon Based Nanocomposites. *ChemEngineering* **2019**, *3* (2), No. 55.

(21) Yan, Z.; Zhu, B.; Yu, J.; Xu, Z. Effect of Calcination on Adsorption Performance of Mg−Al Layered Double Hydroxide Prepared by a Water-in-Oil Microemulsion Method. *RSC Adv.* **2016**, *6* (55), 50128−50137.

(22) Gong, M.; Dai, H. A Mini Review of NiFe-Based Materials as Highly Active Oxygen Evolution Reaction Electrocatalysts. *Nano Res.* **2015**, *8* (1), 23−39.

(23) Li, C.; Wei, M.; Evans, D. G.; Duan, X. Recent Advances for Layered Double Hydroxides (LDHs) Materials as Catalysts Applied in Green Aqueous Media. *Catal. Today* **2015**, *247*, 163−169.

(24) Liang, R.; Tian, R.; Liu, Z.; Yan, D.; Wei, M. Preparation of Monodisperse Ferrite Nanocrystals with Tunable Morphology and Magnetic Properties. *Chem. Asian J.* **2014**, *9* (4), 1161−1167.

(25) Fan, Q.; Li, X.; Yang, Z.; Han, J.; Xu, S.; Zhang, F. Double-Confined Nickel Nanocatalyst Derived from Layered Double Hydroxide Precursor: Atomic Scale Insight into Microstructure Evolution. *Chem. Mater.* **2016**, *28* (17), 6296−6304.

(26) Abello, S.; Verboekend, D.; Bridier, B.; Perez-Ramirez, J. Activated Takovite Catalysts for Partial Hydrogenation of Ethyne, Propyne, and Propadiene. *J. Catal.* **2008**, *259* (1), 85−95.

(27) Zhao, Y.; Zhao, B.; Liu, J.; Chen, G.; Gao, R.; Yao, S.; Li, M.; Zhang, Q.; Gu, L.; Xie, J.; Wen, X.; Wu, L.; Tung, C.; Ma, D.; Zhang, T. Oxide-Modified Nickel Photocatalysts for the Production of Hydrocarbons in Visible Light. *Angew. Chem., Int. Ed.* **2016**, *55* (13), 4215−4219.

(28) Manzi-Nshuti, C.; Wang, D.; Hossenlopp, J. M.; Wilkie, C. A. Aluminum-Containing Layered Double Hydroxides: The Thermal, Mechanical, and Fire Properties of (Nano)Composites of Poly-(Methyl Methacrylate). *J. Mater. Chem.* **2008**, *18* (26), 3091.

(29) Cai, J.; Heng, H. M.; Hu, X. P.; Xu, Q. K.; Miao, F. A Facile Method for the Preparation of Novel Fire-Retardant Layered Double Hydroxide and Its Application as Nanofiller in UP. *Polym. Degrad. Stab.* **2016**, *126*, 47−57.

(30) Gao, Y.; Wu, J.; Wang, Q.; Wilkie, C. A.; O'Hare, D. Flame Retardant Polymer/Layered Double Hydroxide Nanocomposites. *J. Mater. Chem. A Mater.* **2014**, *2* (29), 10996−11016.

(31) Hu, X.; Zhu, X.; Sun, Z. Fireproof Performance of the Intumescent Fire Retardant Coatings with Layered Double Hydroxides Additives. *Constr Build Mater.* **2020**, *256*, No. 119445.

(32) Murtaza, H.; Zhao, J.; Tabish, M.; Wang, J.; Mubeen, M.; Zhang, J.; Zhang, S.; Fan, B. Protective and Flame-Retardant Bifunctional Epoxy-Based Nanocomposite Coating by Intercomponent Synergy between Modified CaAl-LDH and RGO. *ACS Appl. Mater. Interfaces* **2024**, *16* (10), 13114−13131.

(33) Hobbs, C.; Jaskaniec, S.; McCarthy, E. K.; Downing, C.; Opelt, K.; Güth, K.; Shmeliov, A.; Mourad, M. C. D.; Mandel, K.; Nicolosi, V. Structural Transformation of Layered Double Hydroxides: An in Situ TEM Analysis. *npj 2D Mater. Appl.* **2018**, *2* (1), 4.

(34) He, S.; An, Z.; Wei, M.; Evans, D. G.; Duan, X. Layered Double Hydroxide-Based Catalysts: Nanostructure Design and Catalytic Performance. *Chem. Commun.* **2013**, *49* (53), 5912−5920.

(35) Xu, M.; Wei, M. Layered Double Hydroxide-Based Catalysts: Recent Advances in Preparation, Structure, and Applications. *Adv. Funct. Mater.* **2018**, *28*, No. 1802943.

(36) Gabriel, R.; De Carvalho, S. H. V.; da Silva Duarte, J. L.; Oliveira, L. M. T. M.; Giannakoudakis, D. A.; Triantafyllidis, K. S.; Soletti, J. I.; Meili, L. Mixed Metal Oxides Derived from Layered Double Hydroxide as Catalysts for Biodiesel Production. *Appl. Catal., A* **2022**, *630*, No. 118470.

(37) Yang, L.; Liu, Z.; Zhu, S.; Feng, L.; Xing, W. Ni-Based Layered Double Hydroxide Catalysts for Oxygen Evolution Reaction. *Mater. Today Phys.* **2021**, *16*, No. 100292.

(38) Nakazato, R.; Matsumoto, K.; Yamaguchi, N.; Cavallo, M.; Crocella, V.; Bonino, F.; Quintelier, M.; Hadermann, J.; Rosero-navarro, N. C.; Miura, A.; Tadanaga, K. CO_2 Electrochemical Reduction with Zn-Al Layered Double Hydroxide-Loaded Gas-Diffusion Electrode. *Electrochemistry* **2023**, *91* (9), No. 097003.

(39) Mousty, C.; Prevot, V. Advances in Layered Double Hydroxide-Based Materials for CO_2 Electroreduction: A Comprehensive Review of Recent Research Progress. *Appl. Clay Sci.* **2024**, *253*, No. 107362.

(40) Gao, Z.; Lu, L.; Shi, C.; Qian, X.; Wang, X.; Zhang, G.; Zhou, M.; Pan, Y. The Study of ZnAl and ZnFe Layered Double Hydroxide on the Catalytic Dechlorination and Fire Safety of Polyvinyl Chloride. *J. Therm Anal Calorim* **2020**, *140* (1), 115−123.

(41) Khanal, S.; Lu, Y.; Jin, D.; Xu, S. Effects of Layered Double Hydroxides on the Thermal and Flame Retardant Properties of Intumescent Flame Retardant High Density Polyethylene Composites. *Fire Mater.* **2022**, *46* (1), 107−116.

(42) El Khanchaoui, A.; Sajieddine, M.; Mansori, M.; Essoumhi, A. Calcined ZnAl-LDH Trapping Performance in Alginate Beads for Adsorption of Congo Red Dye. *Int. J. Environ. Anal Chem.* **2023**, *103* (18), 6646−6661.

(43) Suárez-Quezada, M.; Romero-Ortiz, G.; Samaniego-Benítez, J. E.; Suárez, V.; Mantilla, A. H_2 Production by the Water Splitting Reaction Using Photocatalysts Derived from Calcined ZnAl LDH. *Fuel* **2019**, *240*, 262−269.

(44) Yan, L.; Yang, K.; Shan, R.; Yu, H.; Du, B. Calcined ZnAl- and Fe_3O_4/ZnAl−Layered Double Hydroxides for Efficient Removal of $Cr^{(vi)}$ from Aqueous Solution. *RSC Adv.* **2015**, *5* (117), 96495−96503.

(45) Liu, J.; Song, J.; Xiao, H.; Zhang, L.; Qin, Y.; Liu, D.; Hou, W.; Du, N. Synthesis and Thermal Properties of ZnAl Layered Double Hydroxide by Urea Hydrolysis. *Powder Technol.* **2014**, *253*, 41−45.

(46) Asghar, H.; Maurino, V.; Iqbal, M. A. Development of Highly Photoactive Mixed Metal Oxide (MMO) Based on the Thermal Decomposition of ZnAl-NO_3-LDH. *Eng.* **2024**, *5* (2), 589−599.

(47) Matsuda, K.; Okuda, A.; Iio, N.; Tarutani, N.; Katagiri, K.; Inumaru, K. Chemical and Structural Transformations of M-Al-CO_3 Layered Double Hydroxides (M = Mg, Zn, or Co, M/Al = 2) at Elevated Temperatures: Quantitative Descriptions and Effect of Divalent Cations. *Inorg. Chem.* **2024**, *63* (34), 15634−15647.

(48) Rauch, E. F.; Veron, M. Coupled Microstructural Observations and Local Texture Measurements with an Automated Crystallographic Orientation Mapping Tool Attached to a Tem. *Materwiss Werksttech* **2005**, *36* (10), 552−556.

(49) Rauch, E. F.; Dupy, L. Rapid Spot Diffraction Patterns Identification through Template Matching. *Arch. Metall. Mater.* **2005**, *50*, 87−99.

(50) Jin, L.; Zhou, X.; Wang, F.; Ning, X.; Wen, Y.; Song, B.; Yang, C.; Wu, D.; Ke, X.; Peng, L. Insights into Memory Effect Mechanisms of Layered Double Hydroxides with Solid-State NMR Spectroscopy. *Nat. Commun.* **2022**, *13* (1), 6093.

(51) Wang, C.; Zhang, R.; Miao, Y.; Xue, Q.; Yu, B.; Gao, Y.; Han, Z.; Shao, M. Preparation of LDO@TiO_2 Core-Shell Nanosheets for Enhanced Photocatalytic Degradation of Organic Pollutions. *Dalton Trans.* **2021**, *50*, 17911−17919.

(52) Rossouw, D.; Burdet, P.; De La Peña, F.; Ducati, C.; Knappett, B. R.; Wheatley, A. E. H.; Midgley, P. A. Multicomponent Signal Unmixing from Nanoheterostructures: Overcoming the Traditional Challenges of Nanoscale X-Ray Analysis via Machine Learning. *Nano Lett.* **2015**, *15*, 2716−2720.

(53) Azar, B. E.; Ramazani, A.; Fardood, S. T.; Morsali, A. Green Synthesis and Characterization of $ZnAl_2O_4$@ZnO Nanocomposite and Its Environmental Applications in Rapid Dye Degradation. *Optik* **2020**, *208*, No. 164129.

(54) Suwanboon, S.; Amornpitoksuk, P.; Rattana, T.; Randorn, C. Investigation of G-C_3N_4/$ZnAl_2O_4$ and ZnO/$ZnAl_2O_4$ Nanocomposites: From Synthesis to Photocatalytic Activity of Pollutant Dye Model. *Ceram. Int.* **2020**, *46* (14), 21958−21977.

(55) Motloung, S. V.; Kumari, P.; Koao, L. F.; Motaung, T. E.; Hlatshwayo, T. T.; Mochane, M. J. Effects of Annealing Time on the Structure and Optical Properties of $ZnAl_2O_4$/ZnO Prepared via Citrate Sol-Gel Process. *Mater. Today Commun.* **2018**, *14*, 294−301.

(56) Chen, Z.; Zhao, X.; Wei, S. Comparative Study on Sol-Gel Combined with a Hydrothermal Synthesis of $ZnAl_2O_4$ and ZnO/$ZnAl_2O_4$ Nanocomposites and Its Photoluminescence Properties and Antibacterial Activity. *Optik (Stuttg)* **2021**, *242*, No. 167151.

(57) Zhao, X.; Wang, L.; Xu, X.; Lei, X.; Xu, S.; Zhang, F. Fabrication and Photocatalytic Properties of Novel ZnO/$ZnAl_2O_4$ Nanocomposite with $ZnAl_2O_4$ Dispersed inside ZnO Network. *AIChE J.* **2012**, *58* (2), 573−582.

(58) Guan, M. Y.; Xu, D. M.; Song, Y. F.; Guo, Y. ZnO/$ZnAl_2O_4$ Prepared by Calcination of ZnAl Layered Double Hydroxides for Ethanol Sensing. *Sens Actuators B Chem.* **2013**, *188*, 1148−1154.

(59) Elam, J. W.; George, S. M. Growth of Zno/Al_2O_3 Alloy Films Using Atomic Layer Deposition Techniques. *Chem. Mater.* **2003**, *15* (4), 1020−1028.

(60) Law, M.; Greene, L. E.; Radenovic, A.; Kuykendall, T.; Liphardt, J.; Yang, P. ZnO-Al_2O_3 and ZnO-TiO_2 Core - Shell Nanowire Dye-Sensitized Solar Cells. *J. Phys. Chem. B* **2006**, *110*, 22652−22663.

(61) Huízar-Padilla, E.; Guillén-Bonilla, H.; Guillén-Bonilla, A.; Rodríguez-Betancourtt, V. M.; Sánchez-Martínez, A.; Guillen-Bonilla, J. T.; Gildo-Ortiz, L.; Reyes-Gómez, J. Synthesis of $ZnAl_2O_4$ and Evaluation of the Response in Propane Atmospheres of Pellets and Thick Films Manufactured with Powders of the Oxide. *Sensors* **2021**, *21* (7), No. 2362.

(62) Ye, A.; Li, Z.; Ding, J.; Xiong, W.; Huang, W. Synergistic Catalysis of Al and Zn Sites of Spinel $ZnAl_2O_4$ Catalyst for CO Hydrogenation to Methanol and Dimethyl Ether. *ACS Catal.* **2021**, *11* (15), 10014−10019.

(63) Lunkenbein, T.; Schumann, J.; Behrens, M.; Schlögl, R.; Willinger, M. G. Formation of a ZnO Overlayer in Industrial Cu/ZnO/Al2O3 Catalysts Induced by Strong Metal-Support Interactions. *Angew. Chem.* **2015**, *127* (15), 4627−4631.

(64) Seto, Y.; Ohtsuka, M. ReciPro: Free and Open-Source Multipurpose Crystallographic Software Integrating a Crystal Model Database and Viewer, Diffraction and Microscopy Simulators, and Diffraction Data Analysis Tools. *J. Appl. Crystallogr.* **2022**, *55*, 397−410.

(65) Finger, L. W.; Hazen, R. M. Crystal Structure and Compression of Ruby to 46 Kbar. *J. Appl. Phys.* **1978**, *49* (5826), 5823.

(66) Sudare, T.; Tamura, S.; Tanaka, H.; Hayashi, F.; Teshima, K. Highly Crystalline Ni-Co Layered Double Hydroxide Fabricated via Topochemical Transformation with a High Adsorption Capacity for Nitrate Ions. *Inorg. Chem.* **2019**, *58*, 15710−15719.

(67) Tsybulya, S. V.; Soloveva, L. P.; Plyasova, L. M.; Krivoruchko, O. P. The Study of Non-Stoichiometric Spinels by Profile Analysis. II.Refinement of the Cationic Distribution in Non-Stoichiometric Al-Zn Spinel. *Zh. Strukt. Khim.* **1991**, *32*, 86−89.

(68) Straumanis, M. E. The Precision Determination of Lattice Constants by the Powder and Rotation Crystal Methods and Applications. *J. Appl. Phys.* **1949**, *20*, 726−734.

(69) Jette, E. R.; Foote, F. Precision Determination of Lattice Constants. *J. Chem. Phys.* **1935**, *3*, 605−616.

(70) Aminoff, G. Ueber Lauephotogramme Und Struktur von Zinkit. *Zeitschrift fuer Kristallographie, Kristallgeometrie, Kristallphysik, Kristallchemie* **1921**, *56*, 495−505.

(71) de la Peña, F.; Prestat, E.; Lähnemann, J.; Tonaas Fauske, V.; Burdet, P.; Jokubauskas, P.; Furnival, T.; Francis, C.; Nord, M.; Ostasevicius, T.; MacArthur, K. E.; Johnstone, D. N.; Sarahan, M.; Taillon, J.; Aarholt, T.; Migunov, V.; Eljarrat, A.; Caron, J.; Nemoto, T.; Poon, T.; Mazzucco, S.; Tappy, N.; Cautaerts, N.; Somnath, S.; Slater, T.; Walls, M.; pietsjoh *Hyperspy/Hyperspy: V2.2.0*; Zenodo: 2024. .

(72) Johnstone, D.; Crout, P.; Francis, C.; Nord, M.; Laulainen, J.; Høgås, S.; Opheim, E.; Prestat, E.; Martineau, B.; Bergh, T.; Cautaerts, N.; Ånes, H. W.; Smeets, S.; Femoen, V. J.; Ross, A.; Broussard, J.; Huang, S.; Collins, S.; Furnival, T.; Jannis, D.; Hjorth, I.; Jacobsen, E.; Danaie, M.; Herzing, A.; Poon, T.; Dagenborg, S.; Bjørge, R.; Iqbal, A.; Morzy, J.; Doherty, T.; Ostasevicius, T.; Thorsen, T. I.; von Lany, M.; Tovey, R.; Vacek, P. *Pyxem/Pyxem: V0.19.1*; Zenodo. .